



UNIVERSITY OF LEEDS

This is a repository copy of *An investigation into the influence of tribological parameters on the operation of sliding triboelectric nanogenerators*.

White Rose Research Online URL for this paper:
<https://eprints.whiterose.ac.uk/172288/>

Version: Accepted Version

Article:

Armitage, JL orcid.org/0000-0002-3092-7929, Ghanbarzadeh, A orcid.org/0000-0001-5058-4540, Wang, C orcid.org/0000-0002-4301-3974 et al. (1 more author) (2021) An investigation into the influence of tribological parameters on the operation of sliding triboelectric nanogenerators. *Tribology International*, 155. 106778. ISSN 0301-679X

<https://doi.org/10.1016/j.triboint.2020.106778>

© 2020 Elsevier. This manuscript version is made available under the CC-BY-NC-ND 4.0 license <http://creativecommons.org/licenses/by-nc-nd/4.0/>.

Reuse

This article is distributed under the terms of the Creative Commons Attribution-NonCommercial-NoDerivs (CC BY-NC-ND) licence. This licence only allows you to download this work and share it with others as long as you credit the authors, but you can't change the article in any way or use it commercially. More information and the full terms of the licence here: <https://creativecommons.org/licenses/>

Takedown

If you consider content in White Rose Research Online to be in breach of UK law, please notify us by emailing eprints@whiterose.ac.uk including the URL of the record and the reason for the withdrawal request.



eprints@whiterose.ac.uk
<https://eprints.whiterose.ac.uk/>

An Investigation into the Influence of Tribological Parameters on the Operation of Sliding Triboelectric Nanogenerators

JL Armitage^{a,b,*}, A Ghanbarzadeh^a, C Wang^a and A Neville^{a,b}

^aInstitute of Functional Surfaces (iFS), School of Mechanical Engineering, University of Leeds, Woodhouse Ln, Leeds LS2 9JT

^bCenter for Doctoral Training in integrated Tribology (iT-CDT), University of Sheffield, Sir Frederick Mappin Building, Mappin Street, Sheffield, S13DS

ARTICLE INFO

Article history:

Received 00 December 00

Keywords:

Triboelectric Nanogenerator
Contact Electrification
Surface Topography
Tribology

ABSTRACT

The triboelectric effect – also known as contact electrification – has long been described as the phenomenon of electronic charge transfer between material surfaces arising purely as a result of mechanical contact. Triboelectric nanogenerators (TENGs) are a series of devices that couple contact electrification and electrostatic induction for applications in various power solutions. The tribological properties of these devices have often been overlooked. Through the development of a novel test apparatus, a clear difference can be distinguished in output current and contact charge accumulation as different insulating and conductive materials are used. A relationship between the rms slope (Rdq) of contacting surfaces and their respective charging rates via triboelectrification is also demonstrated.

1. Introduction

1.1. The triboelectric effect

Historically it has been known that when the surfaces of two differing materials are brought into contact with each other a finite electrical charge is transferred across the interface [1–3]. In almost all situations this charge transfer is propagated through the thermodynamic movement of electrons from occupied high energy states (HOMO / valence band) of one surface into the unoccupied low energy states of the counter-surface (LUMO / conductance band). This movement is driven by a contact potential difference (CPD) proportional to the state densities and energy distributions of the two respective surfaces [4–6]. This CPD is caused by the difference in Fermi level (E_F) for conductive surfaces and ‘effective Fermi level’ ($\langle E_1 \rangle$) for insulators. The ‘effective Fermi level’ for an insulator is defined as being situated within the energy gap between their acceptor and donor states. The cases for conductor-insulator contact and insulator-insulator contact are depicted visually in Fig. 1, as originally described in Matsusaka et al. [5]. Any charge transferred to an insulating surface is confined and accumulates there, instead of immediately being dissipated away through the bulk material as it would in a conductor. The polarity of any charges retained on insulating surfaces after contact is entirely dependent on the direction of flow of electrons during contact, which is in turn dependant on the polarity of the CPD that drives the flow. This phenomenon of charge accumulation on contacting insulator surfaces is often called contact electrification, or contact charging, and has long been observed [7]. When the two materials in contact are also in relative lateral motion to each other, the dynamic variant of contact electrification that occurs is known as frictional electrification or tribo-charging [8]. ‘Triboelectrification’ will be used as an umbrella term to describe these processes throughout this article.

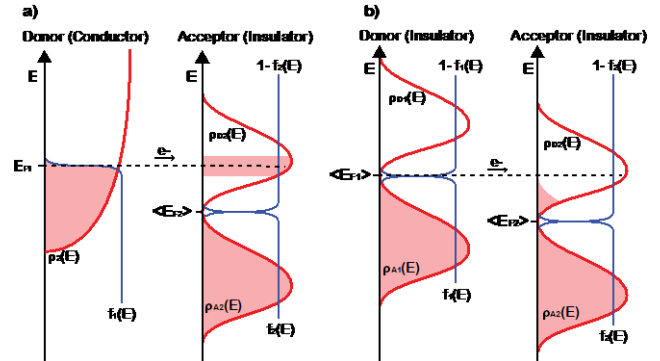


Fig. 1 – Depicting the transference of charge between a metal and an insulator (a), and the transference of charge between two insulators (b). The Fermi level and effective Fermi levels are denoted by E_{Fn} and $\langle E_{Fn} \rangle$ respectively. Fermi-Dirac energy distributions are described by $f_n(E)$ and state densities are described by $\rho_n(E)$ with **A** and **D** denoting acceptor and donator states respectively.

Previous attempts to investigate the triboelectric properties of materials have been mostly qualitative, only being able to identify the polarity of charges developing on material surfaces. These studies allowed for a ‘triboelectric series’ to be produced, where materials are organised into a list in order of the charges they generate on their surfaces [9]. Certain polymers have historically been identified as materials capable of generating the largest CPDs against control counter-materials in the attempts to create a more quantitative triboelectric series [10,11]. This is primarily due to their relative ease for accommodating various functional groups within their structure, allowing for their dielectric properties and surface polarisations to be highly tailored [12]. A good understanding has been established of the electron transfer mechanism [13,14], including relationships between material parameters, transferred charge, and environmental parameters such as temperature and external electric field [3,15,16]. However, the mechanisms underlying the more dynamic aspects of triboelectrification and their roles in application remain to be fully understood.

1.2. Triboelectric nanogenerators (TENGs)

Triboelectric charge transfer and accumulation can have unwanted and even dangerous impacts within various engineering applications; including but not limited to nanoscale electronics [17,18], microscale powder-handling systems [5], macroscale fuel-transport [19], and aerospace applications [20]. However, this accumulation of charge can instead be beneficial for some applications. The most prominent areas for possible applications are in harnessing the relative movement of accumulated contact charges for power generation, and self-powered sensing via electrostatic induction [21,22]. Triboelectric nanogenerators (TENGs) have previously been proposed as a solution for low frequency energy harvesting and sensing [23], since the electrostatic force exerted on a charge is independent of its velocity in accordance with Coulomb's law [24]; as opposed to the electromagnetic force in accordance with the Biot-Savart law [25]. In principle they generate charge densities on the surfaces of contacting components through triboelectrification, which then drive a current through an external circuit via electrostatic induction as they move relative to each other. The properties of this current are primarily dependent on three main physical factors of the device: the relative movement of the charged components (proximity, velocity, acceleration etc.), the surface – or even bulk – charge density of the involved components, and how these surface charges interact with their surrounding environment (charge dissipation, reactions etc.) [26]. These factors are ignoring the properties of any external circuit through which the TENG would be driving this output current.

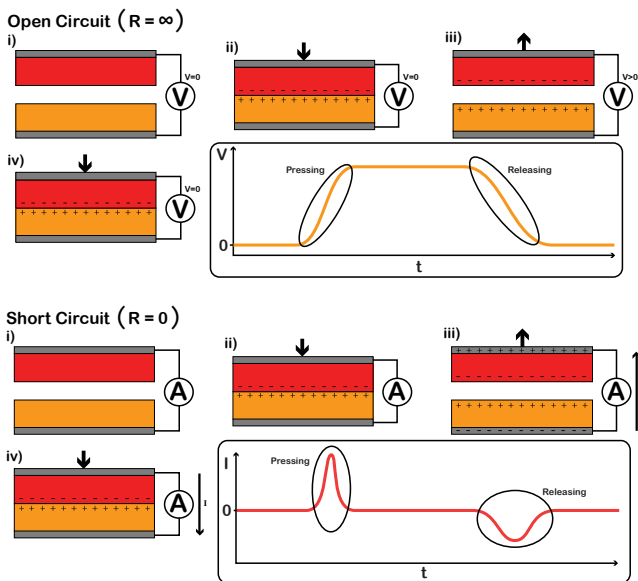


Fig. 2 – Depicting the operation of a contact-separation mode TENG operating in open-circuit (top) and short-circuit mode (bottom). Grey blocks denote a conductive material whereas orange and red blocks denote electropositive and electronegative insulators respectively.

1.3. Device orientation

TENGs have the capability of being very flexible in terms of device construction. The only requirement is at least one material interface – with at least one surface capable of accumulating and retaining electrostatic charges through triboelectrification – and an external circuit capable of detecting the relative movement of surface charges within this interface [27]. Normally this external circuit is in the form of a conductive plate, electronically connected to a ground through some form of power management circuit. This can similarly be achieved through a pair of identical conductive plates connected to each other through a power management circuit. The triboelectric elements of a TENG are either applied to the conductive plates of the output circuit as a form of coating or – conversely – the electrodes are applied to the back of the triboelectric element(s) as a form of conductive coating [29]. The conductive elements can also be their own triboelectric component by being brought into and out

of contact with one particular insulating surface, or by oscillating periodically between multiple surfaces to induce a current through the external circuit [28].

Previous literature has identified four main classes or ‘modes’ of TENG device: vertical contact-separation, lateral sliding, single-electrode, and freestanding triboelectric-layer [27]. These four categories however overlap, as it is possible to construct freestanding triboelectric layer TENGs where the freestanding layer can operate in either contact-separation or lateral sliding mode – or even both [29]. A more logical convention for the classification of TENG devices would be to first classify the mode of motion involved in triboelectrification and the corresponding electrostatic induction of charges (e.g. contact separation, lateral sliding, etc.), and secondly to classify the orientation of the triboelectric elements relative to the external circuit (e.g. attached electrode, single electrode, freestanding triboelectric layer etc.).

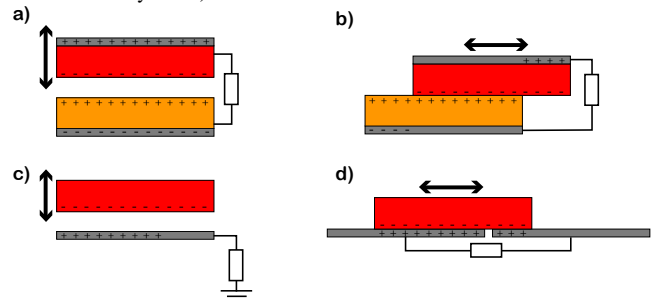


Fig. 3 – Depicting the four initial modes of operation for TENG devices; vertical contact-separation (a), lateral sliding (b), single-electrode (c), and freestanding triboelectric-layer (d) – as originally described by [30].

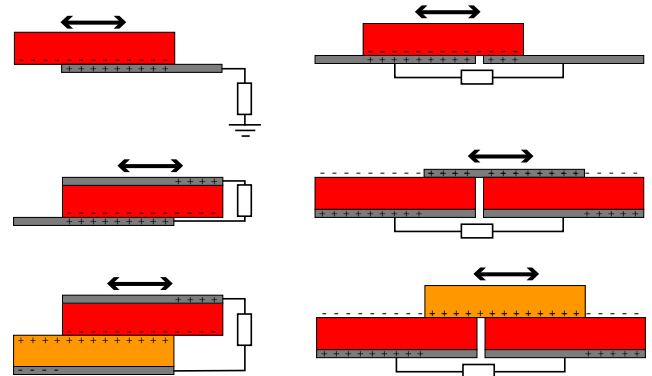


Fig. 4 – Depicting several possible sliding-mode TENG constructions, including single-electrode (top left), attached-electrode (middle left and bottom left), and freestanding triboelectric layer (right) modes. The layout chosen for this methodology is the design to the top right.

1.4. The tribology of TENGs

Much research has been conducted on the electrical properties of TENGs [27], but the mechanical properties eluding to the longevity of these devices are often overlooked due to the low contact pressures that occur within most current TENG applications [31,32]. However, since triboelectric elements in TENG devices are often composed of polymers, the influence of extended periods of operation on device output should be the subject of further investigation. One reason why this is significant is primarily because most bulk polymers exhibit a low material hardness and elastic moduli, which in turn usually leads to undesirable mechanical and tribological behaviours – such as material wear and degradation [33]. Polymers are specifically known to develop transfer layers on harder surfaces within tribological contacts as polymer wear debris is adhered to the counter-surface [34].

This development of a polymer transfer layer within the triboelectric contact presents an interesting tribological problem. In many tribological applications a transfer film is useful in terms of lowering the coefficient of friction within the contact and preventing further wear [35]. The presence of a transfer layer can however inhibit and prevent triboelectric charges from being transferred across the contact interface. As one material is transferred across the contact and adhered to the counter-surface, the thermodynamic drive behind this charge transfer is reduced, since both the occupied and unoccupied electron energy states across the contact is almost identical. An ideal material choice for these triboelectric contacts would be able to maintain this favourable electronic structure whilst simultaneously minimizing material wear. The tribological phenomenon of material transfer layer development has not been previously investigated in the context of TENG durability.

Furthermore, the majority of research into the mechanical aspects of TENGs is conducted solely on contact-separation mode devices. This remains important in terms of assessing the role of adhesion in the wear of triboelectric elements. However little attention has been given to lateral-sliding mode TENGs and how the role of shear stress within the triboelectric contact affects both charge accumulation and material wear. In addition to taking into account how tribological factors affect the operation of TENGs, the role of tribology in the specific mechanisms behind triboelectric charge transfer is also in need of further investigation. It has previously been theorised that frictional excitation can enhance triboelectric charge transfer through phonon-electron interactions [13]. Although giving a detailed and conclusive theoretical analysis of phonon-electron interactions, the experimental validation provided by Pan & Zhang [13] is self-admittedly primitive. This research aims to reinforce this experimental validation, whilst also presenting an insight into the triboelectric behaviour of laterally sliding surfaces.

2. Methodology

A novel apparatus has been designed and tested at the University of Leeds, capable of replicating a macroscale TENG application, providing an insight into how the tribology of triboelectric charge transfer can influence the operation of TENG devices. The tribological tests involving the use of this apparatus have been conducted as a rudimentary way of investigating the roles of surface chemical composition and roughness parameters in triboelectric charge transfer. The apparatus is composed of two main sections; the tribological contact, and the electronic measurement circuit.

2.1. Tribological contact

The tribological contact is constructed to replicate the mechanical properties of a TENG device. The device is constructed so that it has the potential to be facilitated within an existing tribometer environment in order to correlate tribological parameters such as contact force and coefficient of friction with triboelectric charge density. The logical choice of orientation is that of the insulator-conductor laterally-sliding freestanding-triboelectric-layer TENG (abbreviated to F-TENG for the remainder of this article) as depicted in Fig. 4 (top-right), since this device can be replicated within the environment of a reciprocating pin-on-plate tribometer. This orientation involves a freestanding insulating layer that slides laterally across the surface of two conductive electrodes in a reciprocating motion between their respective surfaces. The conductive electrodes normally equal the insulating layer in terms of surface dimensions. This is to maximize the contact time throughout the relative movement between electrodes. The surface dimensions of the respective plates are also maximized within the constraints of use within a reciprocating tribometer environment. The reasoning behind maximizing the surface area is based on the hypothesis that the surface charges accumulated within a triboelectric contact reach a certain spatial saturation density; past which they cannot further accumulate. Therefore, in order to maximize the total accumulated charge – and as a result, induce a larger output current – the total contact area has been maximized.

The specific geometry of the F-TENG apparatus consists of two 70 x 50 x 2 mm³ conductive plates secured in place alongside each other – separated by a 1 mm gap of air – along their 70 mm edges by a supporting

structure. These conductive plates are secured to the base of the apparatus via vertical clamps which cover the top and bottom 50 x 10 mm² sides of each electrode. This results in two 50 x 50 mm² surfaces exposed, separated by a 50 mm x 1 mm² air gap. This lower part of the apparatus remains stationary whereas the insulating upper plate reciprocates laterally across the surfaces of the two lower electrodes. The insulating layer for this methodology consists of a 50 x 50 x 20 mm³ block. The vertical clamps designed to hold the lower electrodes in place also guide the movement of the upper layer, preventing it from any perpendicular deviation along the length of the stroke. The supporting structure also provides space underneath the electrodes for secure attachments to the external output measurement circuit. Longer electrodes and freestanding layers can also be accommodated by this apparatus along the stroke length, as well as the lateral spacing of the electrodes.

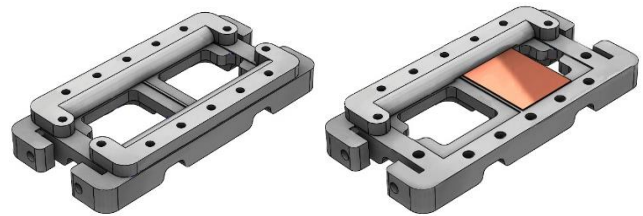


Fig. 5 – Schematic representation of the F-TENG supporting structure without samples (left), and one schematic with one lower sample, one upper clamp removed to show the lower sample holder (right).

2.2. Electronic measurement circuit

The test apparatus used a simple impedance circuit and two electrometers to measure and record the output voltage and current for the F-TENG contact. The reciprocating TENG contact can be represented by an alternating voltage source and a variable capacitor combined in series as described by [27]. The physical contact involves an insulating plate with isolated surface charges reciprocating across the surfaces of two conductive plates. Because of this reciprocating nature, one can expect the output current to alternate corresponding to the velocity profile of the insulating layer relative to the conductive layers. The properties of this alternating current are also strongly dependent on the external circuit through which it is driven. If the external circuit has zero impedance then any induced current will reflect the physical movement of the isolated charges on the insulating surface layer, due to conservation of charge. The voltage across this short-circuit is infinitesimally small due to the relative ease of current flow under Ohm's Law. As a resistance is introduced to the external circuit, it is expected that the current flow becomes impeded and a larger – more sustained – voltage occurs. If an infinite resistance is introduced and an open-circuit case is imposed, then no current would flow between the two plates, however an alternating external voltage would develop every oscillation to counter the physical movement of charge.

If a sufficient balance between output current and voltage is struck through calculation of an optimal resistance value, the output power of the TENG device can be maximized [27]. The introduction of more complex methods of impedance such as capacitors and inductors would have a similar effect on the device output, dependent on the frequency of the physical reciprocation. The measurement circuit, for the tests conducted as part of this investigation, incorporated placing a 10 M Ω resistor between the two conductive TENG plates in parallel to a Keithley 6517B/E electrometer in order to measure and record the voltage across it over time. Another 6517B/E was placed in series with this resistor and the TENG device in order to measure the load current passing through the circuit. The final configuration of the measurement circuit is as described in Fig. 6. This configuration allows for the measurement and recording of both the output current and voltage of the TENG device with regards to a specific load resistance; which can subsequently be changed in order to optimize the output power.

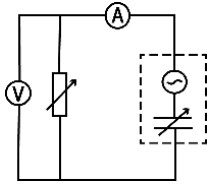


Fig. 6 – Schematic representation of the F-TENG electronic measurement circuit. The two electrometers are denoted as A and V to represent their purpose as ammeter and voltmeter respectively.

2.3. Sample preparation

The conductive electrodes used in these tests were composed of two differing metals in order to compare their triboelectric potentials and correlate to their respective work functions. The two metals used were copper and aluminium. All electrode samples were polished using a grinding and polishing rig, a non-woven nap-free polishing pad, and a diamond suspension in order to attain a consistent low surface roughness across all electrodes. This was to provide a relatively flat counter-surface for the polymer-metal contact for consistency and ease of contact pressure modelling. The insulating polymer blocks used in testing were also composed of differing materials to provide an adequate matrix for material comparison. The three polymers used were Delrin (Polyoxymethylene, POM), Nylon (Polyamide 6-6, PA66) and Teflon (Polytetrafluoroethylene, PTFE). Both Delrin and Nylon have previously been demonstrated to have a high surface energy, making them both strongly electropositive materials which prefer to donate electrons to counter-materials [9]. Teflon however has exhibited a very low surface energy and has been shown to be a very strongly electronegative material that draws electrons from counter materials. Previous research has investigated and emphasised the use of fluorinated polymers such as Teflon, Polyvinylidene Fluoride (PVDF), and Fluorinated Ethylene-Propylene (FEP) for electronegative triboelectric contacts, without investigating electropositive materials to the same extent. These fluoropolymers are already used as surface-active additives for the reduction of surface tension and wettability of polymer matrices [39]. This could be attributed to their relatively high corrosion resistance and low susceptibility to Van der Waals forces. The polymer blocks were also subject to a grinding process using the same apparatus and 600 grit silicon carbide (SiC) grinding pads to approximate a uniform surface across the different polymers and minimise the effects of surface texture on charge generation. SiC grinding pads of differing grit values from 120 up to 1200 were used on the polymer samples to investigate the contribution of differing surface roughness parameters, real contact area, and the distribution of contact pressures to triboelectrification. Additional blocks were also polished using the same method as the electrodes in order to lower their surface roughness as much as possible as a control measure. The surface roughness parameters of both the conductive and insulating samples were measured using a Bruker NPFLEX white light interferometer and are shown in Table 2 and Table 3 respectively. The surface topography height maps for the conductive electrode and polymer sample surfaces are displayed in Appendices A.1. and A.2. respectively.

2.4. Testing procedure

Background measurements were taken for 10 s before beginning every test in order to evaluate the influence of external electrical interference from lighting fixtures and power supplies. These background measurements were taken in the same environment as the tests themselves, only with both electrodes exposed to air within the lower sample holder, instead of one or both being in contact with the insulating upper layer. Once the background noise had been sampled, the insulating block was placed directly onto one electrode – making their surfaces completely overlap – and was immediately oscillated at 2.7 Hz, with an uncertainty of 0.3 Hz. In order to prevent any possible triboelectrification prior to the test start, the insulating layer was not put into stationary contact with the electrodes before the oscillations began. If static triboelectrification was to occur before the test start, the resulting data would not be a reliable representation of how contact charge initially accumulates in a sliding contact environment.

2.5. Post processing

Current and voltage data were collected from the two electrometers in their respective measurement modes and written into a tab delimited .txt format through the use of a National Instruments myDAQ device and specialised LabVIEW software written in-house. An in-house MATLAB code was then used to effectively remove background electrical interference from the raw data and analyse the resulting cleaned data. Background data was identified through a Fourier transform and removed using selective notch filters. Background samples predictably found significant interference at 50 Hz as well as at various harmonic frequencies being emitted from the mains power lines within the testing room. Notch filters were applied at 50, 100, 150 and 200Hz in order to remove this background interference. The effectiveness of this technique is shown in Fig. 7 and Fig. 8.

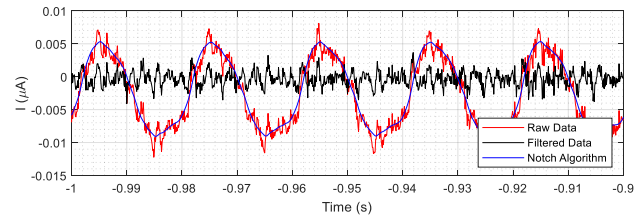


Fig. 7 – Raw induced background current (red) over time, alongside fitted data produced by the four-stage notch filter (blue) and the final filtered data (black).

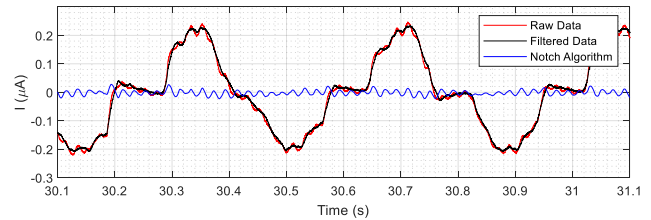


Fig. 8 – Raw induced current (red) over several oscillations during an example test, alongside fitted data produced by the four-stage notch filter (blue) and filtered data (black) to show how the filter discerns between the signal and background noise.

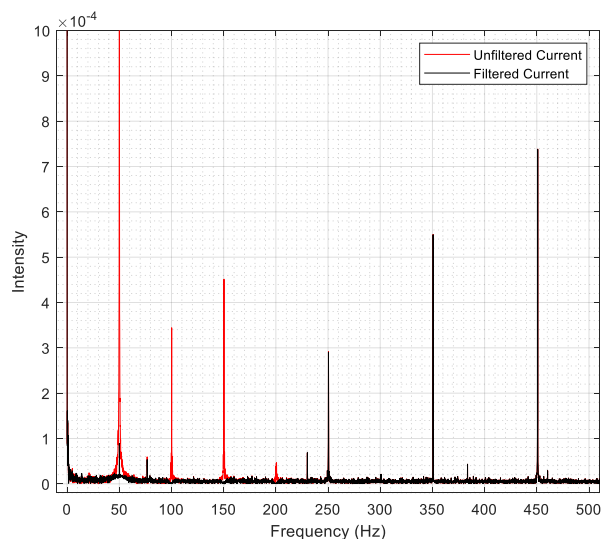


Fig. 9 – Fourier transform of a generic initial 10 s of background raw current (red) induced by external interference; illustrating significant interference at 50 Hz and its even harmonic frequencies. These data were processed through a four-stage notch filter to remove interference at 50Hz and its first three harmonics (black).

A threshold trigger was used within the MATLAB code to identify the start and end of each stroke in order to account for inconsistencies in oscillation frequency, as well as to compare how certain output properties change per oscillation across the duration of each test.

3. Results & Discussion

3.1. Induced current and voltage over time

A current and voltage signal was detected for every F-TENG material combination as the polymer blocks were physically moved across the electrode surfaces. This current and voltage indicated a conductive movement of charge to balance out the physical movement of static charge – and resulting change in electrostatic field – relative to the measurement circuit. The polarity of the current and voltage for each test correlated with that of the theorised charge polarity accumulating on the contacting polymer surface, as well as the direction of the block's movement. The currents and voltages produced by the forward stroke of the POM block had the reverse polarity to those produced by the forward stroke of the PTFE block as shown in Fig. 10. This indicates that the charges developing on their respective surfaces when in contact with identical counter-surfaces are of opposing polarities. More specifically, the polarity of these currents indicated that the PTFE block accumulated a negative surface charge with all counter-surfaces whereas the PA66 and POM blocks accumulated positive surface charges. These charge polarities elude to the respective accumulation and loss of surface electrons for PTFE, and PA66 and POM as the result of their respective lower and higher surface energy levels in agreement with previous research [9].

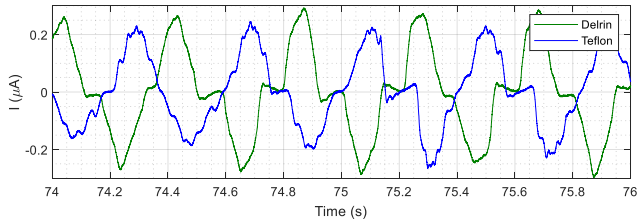


Fig. 10 – Output currents for 50 x 50 mm POM (green), and PTFE (blue) on Aluminium F-TENG contacts reciprocating at 2.7 (± 0.3) Hz for 2 s with a stroke length of 50 mm and a 1 mm lateral electrode spacing. Indicating the reversed polarity of the PTFE current relative to POM.

As the polymer blocks continued to be reciprocated over the electrode surfaces, a pulse-like alternating current was detected – driven by an oscillating voltage – with a frequency correlating to that of the physical motion of the block as shown in Fig. 10. The alternating behaviour of this signal indicates that both the amplitude and polarity of the produced current is also proportional to the velocity of the polymer block relative to the electrodes. This velocity dependent property indicates that the relative movement of the polymer block, with respect to the conductive electrodes, is in fact forcing the movement of electronic charge through the external circuit via electrostatic induction as predicted.

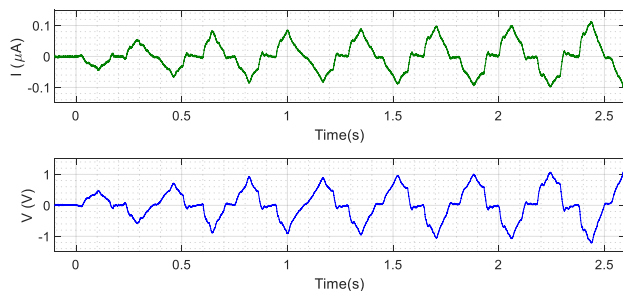


Fig. 11 – Output current (green, top) and voltage (blue, bottom) for 50 x 50 mm PA66 on Copper F-TENG contact reciprocating at 2.7 (± 0.3) Hz for 2.5 s with a stroke length of 50 mm and a 1 mm lateral electrode spacing.

3.2. Contact charge accumulation

Another prominent feature of both the voltage and current outputs was that the amplitude of these alternating signals increases throughout the duration of each test – despite a constant oscillation frequency throughout them. This phenomenon indicates that the charge density on the insulating polymer surface is increasing throughout the duration of the test, which in turn leads to a larger contact potential difference and a larger induced current when moving at the same relative velocity. The contact charge can be evaluated by integrating the current output for each half-oscillation over time in accordance with Coulomb's law. This indirect method of calculation is more suitable for this particular apparatus, as measuring the contact charge directly – and in-situ – via methods such as Kelvin probe force microscopy (KPFM, [36]) is not within the current capabilities of atomic force microscopy.

$$I(t) = \frac{dQ(t)}{dt} \therefore Q_n = \int_{t_n}^{t_{n+1}} I(t) dt \quad (1)$$

In Coulomb's Law the current (I) is described as the time derivative of charge (Q) as it passes through an arbitrary aperture (e.g. the cross-section of a wire). This allows charge to be calculated as an integral of current between two points in time. These two points (t_n, t_{n+1}) being the start and finish of each respective half-oscillation. This integration method is visually represented by Fig. 12. Coulomb's Law also provides an explanation into how the F-TENG apparatus induces current through the physical movement of surface charges. Consider a surface that has a length of w m in the y direction and has a spatial charge density of σ Cm^{-2} . If this surface travels with a velocity of v ms^{-1} in the x direction, the equivalent current of this movement of charge can be calculated by considering the variables and units involved. Multiplying the two-dimensional spatial density by the width of the surface in the y direction will give the one-dimensional spatial density of the surface in the x direction, denoted as λ . Multiplying λ by v will then give a value in Cs^{-1} , which can be interpreted as a current value in Amperes.

$$I \equiv w\sigma v \quad (2)$$

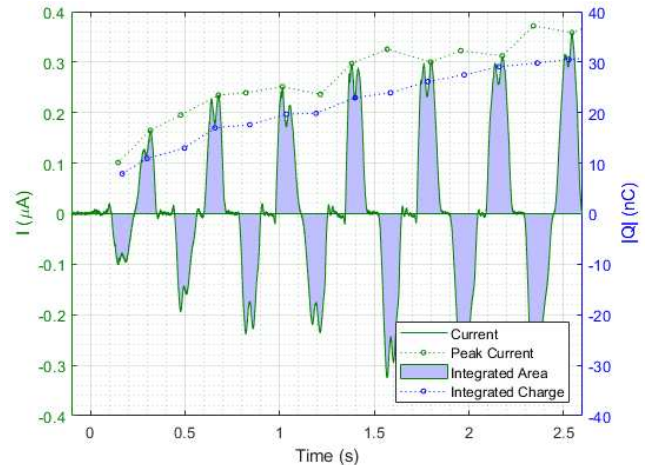


Fig. 12 – Output current (green line, left), maximum output current per half-oscillation (green markers, left), and contact charge per oscillation (blue markers, right) for the first 7 oscillations of a generic F-TENG contact. The blue areas illustrate the integration areas for charge calculation with respect to the left y axis (green).

Upon initial comparison of this contact charge accumulation alongside the maximum output current per oscillation, it becomes clear that this time-integrated value is more reliable for providing information on what is electronically happening within each TENG contact. This is due to the much smaller deviations in value from oscillation to oscillation throughout test durations, as depicted in Fig. 13. This higher consistency arises from the time-integrated property of the measurement, as it mitigates the large errors introduced with inconsistencies in oscillating frequency and velocity

profile of the moving block. A clear pattern is seen in the integrated charge values, showing the contact charge accumulating across the duration of every test. The charging rate for all material pairings also slows as the contact charge density approaches a particular saturation value.

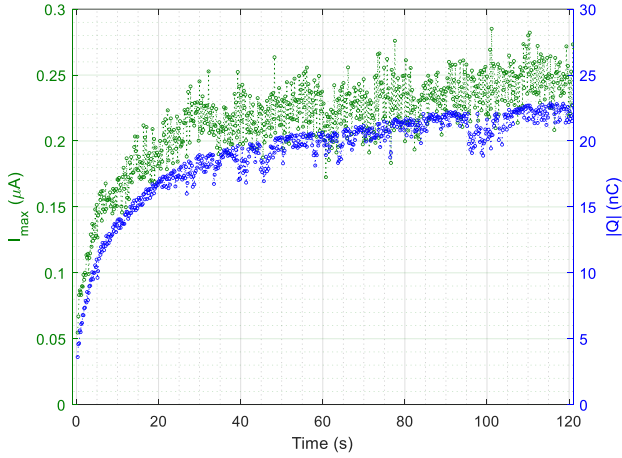


Fig. 13 – Maximum output current per half-oscillation (blue, left), and contact charge per half-oscillation (green, right) for a generic F-TENG contact.

This charging behaviour is the primary reason why TENG devices exhibit capacitive properties [27]. The physical reason behind this behaviour is that as the surface charge density increases, the CPD and resulting charge transfer rate lessens as the states of the acceptor are filled with donor electrons from the counter-material [26]. This contact charge accumulation – being driven by the CPD – via triboelectrification is similar to charge accumulating on either side of a traditional capacitor as an external voltage is applied to it. The relationship between charge (Q) over time (t) for a traditional capacitor with a capacitance of C being charged by a supply voltage V_0 across a circuit with a load resistance of R is described as

$$Q(t) = CV_0 \left(1 - e^{-\frac{t}{RC}}\right) \quad (3)$$

The in-house MATLAB program was adapted to fit this particular function to the charge accumulation data for each test. Two arbitrary constants a and b were assigned to the values of CV_0 and RC respectively. The additional constant c was included to account for any potential offsets in time (t) for the start of each test, giving the following *fittype* in MATLAB.

$$Q(t) = a(1 - e^{-b(t+c)}) \quad (4)$$

The charge accumulation trends shown in the majority of tests using the F-TENG apparatus showed a combination of exponential accumulation – as one would find in a traditional capacitor.

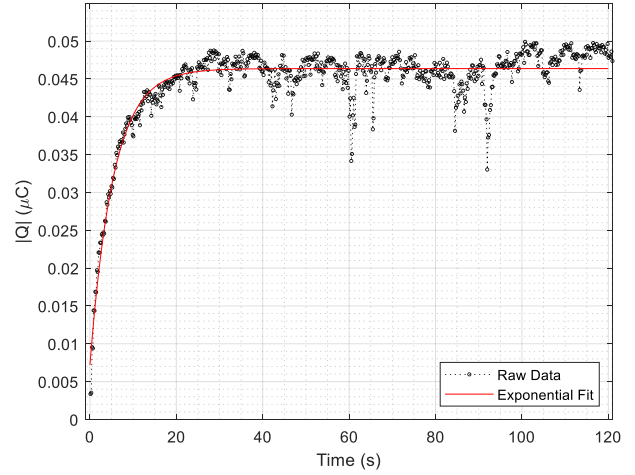


Fig. 14 – Contact charge per half-oscillation (black) fitted against an exponential (red) charging function for a generic F-TENG contact, exhibiting a more exponential charging pattern with an R^2 value of 87.89. The coefficients for the exponential function are as follows: $a = 0.04637 \pm 0.0019$, $b = 0.1849 \pm 0.011$, $c = 0.9141 \pm 0.2591$.

There are points during a number of tests where the integrated value for contact charge drops sharply – either over the course of one half-oscillation or several – and then steadily rises back up over the course of the following seconds. These more abrupt changes may be an indication of dielectric breakdown across the F-TENG contact. Dielectric breakdown in this situation would be caused by it becoming energetically favourable for some transferred electrons to tunnel back to their original material surface as a result of the charge density on the surface they had previously transferred to being close to complete saturation [37]. These abrupt drops in contact charge often accompany changes in the way that current is induced across the stroke of the sliding contact, making the pulse-shape – or effectively waveform – of the alternating current pattern produced by the T-FENG sliding contact another interesting characteristic to examine.

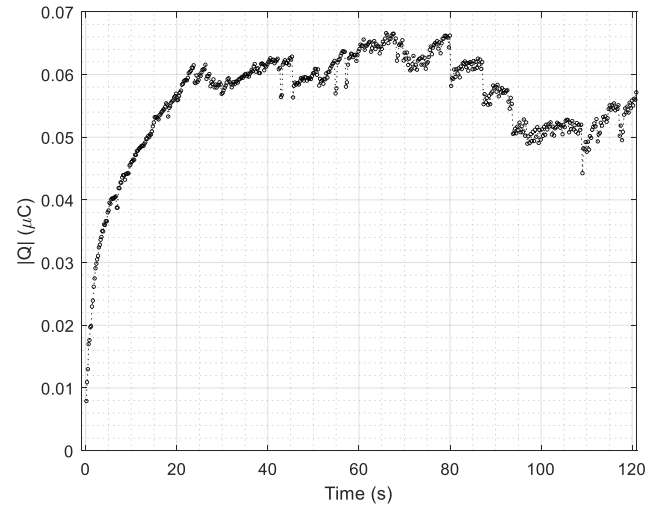


Fig. 15 – An extreme-case example of how contact charge can abruptly drop and attempt to rise back up several times during F-TENG testing. The material combination used for this specific test was PA66 on Copper.

3.3. Cycle characteristics

The alternating current generated by each specific material pairing had varying characteristics in addition to increasing in overall amplitude across the duration of each test. Upon inspection of the current data over time for each test it is apparent that the waveform produced by the oscillatory motion of the polymer block changes at points during each test, as shown in Fig. 16.

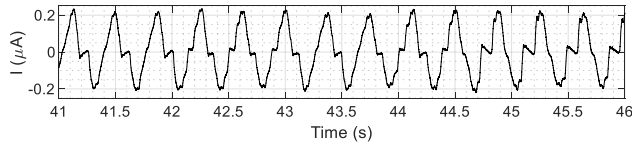


Fig. 16 – An example of how current waveform can change across the duration of a typical F-TENG test.

Three-dimensional line-plots and two-dimensional colour-scaled images have been produced by stacking side-by-side the pulses induced – in both current and voltage – by each forward and reverse stroke respectively throughout each test. The aim of this is to further investigate these changes in wave-shape and to ascertain their origin. This can be seen in Fig. 17 where an overlying pattern in waveform is present across the duration of the test. Whilst an overlying pattern in waveform is seen for all F-TENG tests, these overlying patterns developed and changed progressively across the duration of each individual test. In addition to this, each test exhibited different overlying patterns.

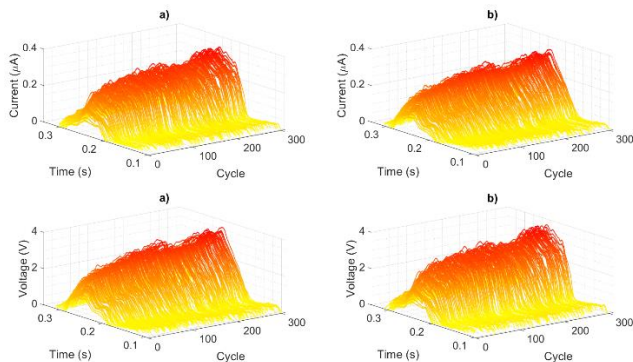


Fig. 17 – 3D colour-scaled line-plot depicting output current (a, b) and voltage (c, d) over time (samples) for each forward (a, c) and reverse stroke (c, d) of the POM on Aluminium F-TENG contact over the duration of the test (cycles); Depicting the changes in current and voltage waveform as the test progressed.

More abrupt changes in waveform and overall amplitude occurred during a number of tests, which persisted for up to dozens of oscillations during testing. These changes in waveform often coincide with changes in the maximum recorded current and voltage values for their respective oscillations. Changes in values calculated using time-dependent integrations such as contact charge coincide with changes in waveform, however some changes in waveform do occur without any changes in contact charge. Fig. 18a is a 2D representation of how the current waveform changes across the same charge accumulation depicted in Fig. 18b. An abrupt change in waveform is observed after approximately 117 oscillations during this particular test, coinciding with a drop in contact charge. These changes in waveform could have a number of causes due to the nature of testing. Changes in velocity profile of the block can lead to a change in how the current is induced across each stroke. Dielectric breakdown within the contact can also cause an abrupt change in CPD and current. Another cause could be geometric changes within the F-TENG apparatus.

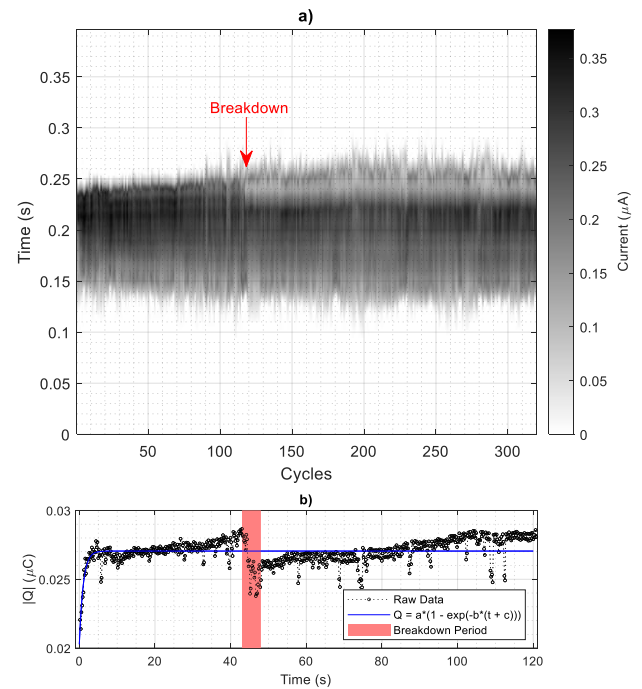


Fig. 18 – a) 2D colour-scaled image depicting output current over time for each forward stroke of a PTFE on Copper F-TENG contact across the duration of an example F-TENG test (cycles). b) Contact charge per cycle across the duration of the same test, highlighting an abrupt change in current waveform and contact charge during the 118th cycle of the test.

A control test was ran to gauge the influence of lateral electrode spacing to find that it did affect the waveform for both current and voltage output. The results for this test are depicted in Fig. 19 and show how the current and voltage waveform becomes more concentrated across the stroke as the electrode spacing increases from 1mm to 10mm gradually across 100 cycles. This change in lateral electrode spacing did also cause a gradual decrease in time-integrated contact charge. This is interesting as a geometric change within the apparatus should only change the waveform rather than also changing the area underneath each pulse. It may be concluded that any changes in current waveform that do not coincide with a change in time-integrated contact charge is a result of a change in sample velocity profile, whereas those that do may be a result of electrostatic discharge within the contact or geometric change within the apparatus.

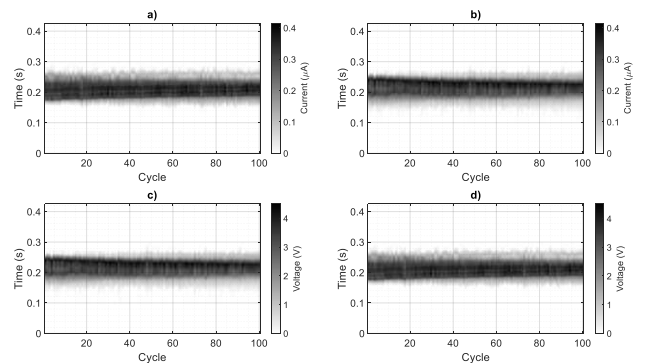


Fig. 19 – 2D colour-scaled equivalent of Fig. 17, depicting output current (a, b) and voltage (c, d) over time (samples) for each forward (a, c) and reverse stroke (c, d) for 100 cycles of an example POM on Aluminium F-TENG contact; Depicting the changes in current and voltage waveform as the lateral electrode spacing is increased from 1mm to 10mm across the test cycles.

3.4. Surface composition

An interesting trend was found upon comparison of the different material pairings in the F-TENG apparatus. As expected, all material pairings with differing compositions exhibited not only different contact charges at the end of each test, but the pairings also reached these charges at differing rates. These data suggest that the surface composition of a material not only has an influence on the maximum charge density it can attain against a given counter-material, but also the rate at which it can accumulate this charge via triboelectrification in a sliding environment. Upon comparison of the three polymer surfaces it is clear that their chemical composition has a significant influence on the maximum amount of charge it can attain via triboelectrification, as well as the rate at which triboelectrification may occur. After 120 s of triboelectrification under the aforementioned F-TENG test conditions the Delrin, Nylon and Teflon surfaces reached contact charges of approximately 25 nC, 49 nC and 23 nC respectively. Of the three polymers used in testing, Nylon accumulated the most charge within the given test time. This emphasises the usefulness of electropositive insulating materials for triboelectric contacts in agreement with [11]. Despite Teflon exhibiting a lower saturation charge density than expected, the Teflon surfaces did all reach their respective saturation densities considerably faster than the Delrin and Nylon surfaces. The charging rates for Teflon surfaces were also much more easily matched to the model for exponential charge accumulation than the Delrin and Nylon surfaces.

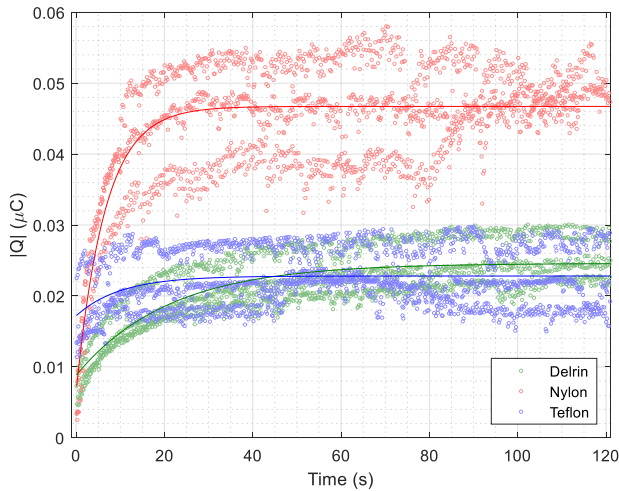


Fig. 20 – Contact charge accumulation over time for POM (green), PA66 (red), and PTFE (blue) on Aluminium F-TENG contacts. Three example tests were taken from each material pairing in order to exhibit the level of consistency and repeatability achieved.

Table 1– Average coefficients for exponential fittings of charge accumulation data for POM, PA66 and PTFE on Aluminium F-TENG tests.

Polymer	a	b	c
Delrin	0.0246	0.048	9.3
Nylon	0.0467	0.154	0.9
Teflon	0.0228	0.1	14

In terms of conductive electrodes, the copper electrodes consistently produced a larger charge density on all counter-materials than the aluminium electrodes. This increase in charge between copper and aluminium electrodes was approximately 12% for Delrin counter-surfaces, 22% for Nylon counter-surfaces, and 27% for Teflon. This is partially contradictory to what was expected of the F-TENG tests, as one would expect the contact charge magnitude and polarity to be determined by the distribution of energy levels and state densities in the respective surfaces.

In this case one would expect Copper to charge electronegative surfaces such as Teflon faster than aluminium, but charge electropositive materials slower than aluminium since Copper has a higher work function. This implies that there are more factors to consider than surface active groups and chemical composition when considering the effectiveness of triboelectric contacts.

3.5. Surface roughness parameters

The primary mechanical factor to consider for TENG contacts is the real contact area. In order to maximise the charge accumulating within a TENG contact it is important to both maximise the charge density per unit surface area within the contact, as well as the real surface area in mechanical contact. An important factor to consider when calculating the real contact area between two interacting surfaces are their respective topographies. The consequence of these variations in surface topography is that the real contact area between two surfaces may be significantly smaller than the apparent contact area [38]. This effect is amplified if the two surface topographies conform less to one another. Materials with higher hardness values and elastic moduli are prone to deform less under contact pressure. This implies that for two polymer surfaces that are generally soft, their low elastic moduli allow them to deform elastically more easily to allow their surfaces to conform with any counter material to a greater extent under the same contact pressure.

F-TENG tests were conducted using Nylon samples of differing surface topographies, produced via the aforementioned grinding technique. The surface topographies of each Nylon sample – as well as the surfaces of each Delrin and Teflon sample – were recorded using a Bruker NPFLEX white-light interferometer. Another in-house MATLAB code was written to analyse the raw ASCII output files produced by the NPFLEX in order to create pixel-by-pixel maps of each surface and evaluate their roughness parameters. In addition to calculating these roughness parameters and mapping the topography of each surface, the MATLAB code is also capable of mapping the gradient magnitude and direction across a scan using MATLAB's *imgradient* function. This can be useful for identifying the directional contributions to a particular roughness profile which may arise from surface finishing processes such as grinding. The centre-line average roughness (R_a) is evaluated as the arithmetic mean height deviation of a surface, as well as through a volumetric integral.

$$R_a = \frac{1}{\Delta x \Delta y} \sum_{i=1}^{n_x} \sum_{j=1}^{n_y} |z_i| \cong \frac{1}{\Delta x \Delta y} \int_0^{\Delta y} \int_0^{\Delta x} |z_i| dx dy \quad (5)$$

Another important surface topography parameter is the rms slope, otherwise known as R_{dq} . This has previously been identified as a key parameter for estimating the real contact area within triboelectric contacts [31], and is described below as the square root of the arithmetic mean deviation in squared gradient across the sample area.

$$R_{dq} = \sqrt{\frac{1}{\Delta x \Delta y} \int_0^{\Delta y} \int_0^{\Delta x} \left[\left(\frac{\partial z(x,y)}{\partial x} \right)^2 + \left(\frac{\partial z(x,y)}{\partial y} \right)^2 \right] dx dy} \quad (6)$$

In addition to mapping the overall height and gradient across sample areas of a surface, two more parameters can also be used to gain a better understanding of the topography; skewness and kurtosis. The skewness of a surface is a measurement of the distribution of surface height around the mean surface height. It identifies whether the defining features of a surface are peaks or valleys. A positive skewness shows that the surface height distribution is skewed above the mean surface height, implying that the surface topography is dominated by valleys and/or pits and vice versa. A positive skewness of a surface may also imply a larger portion of the surface being in real contact with a counter surface than a surface of identical R_a and R_q but a lower skewness value [39]. The skewness of a surface is described mathematically as

$$R_{sk} = \frac{1}{\Delta x \Delta y R_q^3} \sum_{i=1}^{n_x} \sum_{j=1}^{n_y} z_i^3 \cong \frac{1}{\Delta x \Delta y R_q^3} \int_0^{\Delta y} \int_0^{\Delta x} z_i^3 dx dy \quad (7)$$

Kurtosis is a measure of the sharpness of the roughness profile of a surface. A high kurtosis value for a surface implies that the topography is composed of sharp asperities. An exceedingly high kurtosis value for a surface scan may also imply the presence of anomalous values, causing an unusually sharp peak or pit across one pixel of the scan.

$$R_{ku} = \frac{1}{\Delta x \Delta y R_q^4} \sum_{i=1}^{n_x} \sum_{j=1}^{n_y} z_i^4 \cong \frac{1}{\Delta x \Delta y R_q^4} \int_0^{\Delta y} \int_0^{\Delta x} z_i^4 dx dy \quad (8)$$

Table 2 – Surface roughness parameters for conductive electrode plates using a Bruker NPFLEX white light interferometer.

Material	R_a (nm)	R_{dq}	R_{sk}	R_{ku}
Aluminium	16.8	$9.3e^{-3}$	3.03	38.8
Copper	16.8	$8.2e^{-3}$	-0.37	15.1

Upon inspection of the conductive electrode topographies, the higher surface roughness (R_a) and rms slope (R_{dq}) of the aluminium electrodes may constitute towards a smaller true contact area between any counter-surface; which may also in turn explain the lower contact charge values across all counter-materials for the aluminium samples. Both electrode surfaces exhibit a negative skewness, implying that peaks and asperities are their most prominent features. The copper surface scans did also exhibit a high surface kurtosis, implying that the asperities on the copper surface are generally sharper than those on the aluminium surface. This high kurtosis value combined with a negative skewness would normally insinuate that the copper surface would have a smaller true contact area when pressed against a hypothetical counter-surface that is perfectly flat and infinitely hard [39]. However, the low moduli and viscoelastic nature of polymers instead implies that these sharp asperities would instead penetrate the polymer counter-surface and produce a larger contact area across the contact in general [40]. Example surface scans and gradient maps of the aluminium and copper surfaces can be found in A.1. and B.1. respectively. Upon examination of the polymer surfaces, the grit value for the SiC grinding pads used in the grinding process correlates inversely with the centre-line roughness – and negatively with the rms slope – of the resulting Nylon surface topographies. The roughness parameters for each Nylon surface are displayed in Table 3.

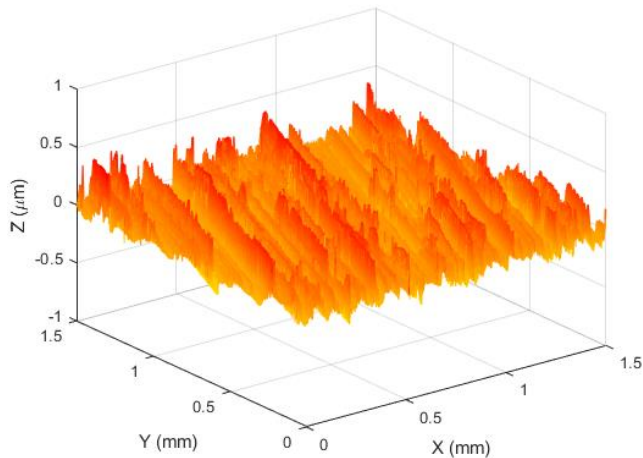


Fig. 21 – Sample 1.5 mm x 1.5 mm surface topography of the Delrin surface after being subjected to a grinding process using 120 grit SiC pads.

Table 3 – Surface roughness parameters for insulating triboelectric layers using a Bruker NPFLEX white light interferometer.

Material	R_a (μm)	R_{dq}	R_{sk}	R_{ku}
Nylon 120 grit	1.56	0.40	-0.08	3.89
Nylon 600 grit	0.61	0.23	0.82	15.90
Nylon 800 grit	0.41	0.22	-0.20	4.69
Nylon 1200 grit	0.24	0.11	2.95	131.31
Nylon Polished	0.13	$5.6e^{-2}$	-0.78	8.04

Upon comparing the charge accumulation data for the Nylon surfaces of differing roughness, a correlation between the 600, 800 and 1200 grit charge accumulation is difficult to discern. However the 120 grit surfaces consistently accumulate charge at a lower rate than any other surface topography; to the point where they do not appear to reach a saturation charge density after two minutes of testing. The polished Nylon surfaces also accumulated charge consistently faster – and to a higher saturation density – than any surface that had only undergone a grinding process. These two cases are true not only for the pairing of Nylon and Aluminium, but for every pairing between the three polymers and two electrode materials. An example comparison between tests using Nylon samples of varying roughness parameters is displayed in Fig. 22. These data may imply that surfaces of lower surface roughness parameters – predominantly rms slope – inherently develop larger charge densities via triboelectrification. However, it may be more accurate to state that the case in fact applies to surfaces that topographically conform to a greater extent with their relative counter-surfaces, owing to the low roughnesses of the electrode surfaces. In turn this may confirm that the larger charge densities are in-fact a partial result of there being a greater real contact area within the F-TENG contact.

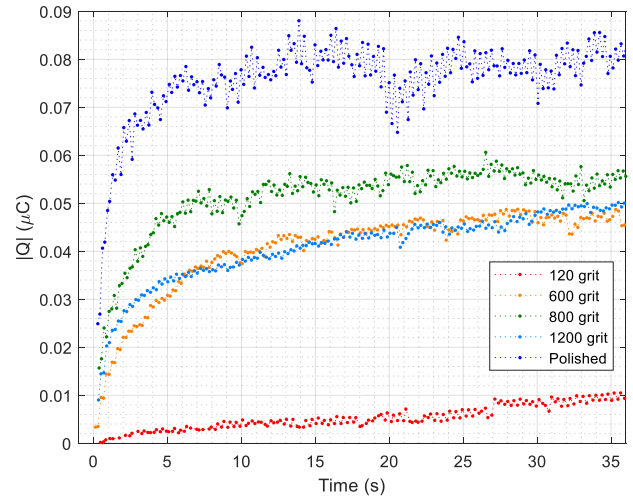


Fig. 22 – Contact charge accumulation over time for PA66 on Aluminium F-TENG contacts using PA66 samples of differing surface roughness.

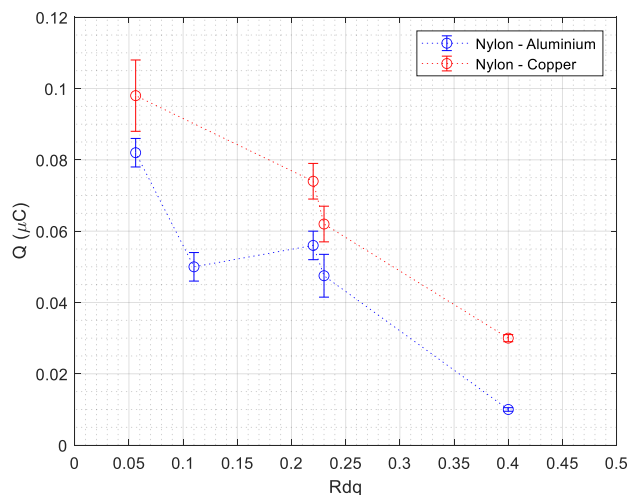


Fig. 23 – Contact charge accumulated over 35 seconds (Q) plotted against polymer surface rms slope (Rdq) for PA66 on Aluminium (blue) and Copper (red) F-TENG tests.

4. Conclusion

In this paper a methodology for investigating the output performance of sliding-freestanding triboelectric layer triboelectric nanogenerators (F-TENGs) is presented. This methodology has provided results in agreement with existing research whilst also describing the tribological viewpoint from which future TENG data can be analysed. These data have shown that charge accumulation for an F-TENG contact exhibits a combination of exponential and logarithmic trends. The saturation charge, charge accumulation rate, in addition to how this rate develops over time as triboelectrification occurs is shown to be dependent on both the surface compositions and surface roughness parameters of the contacting materials. Teflon freestanding layers were shown to accumulate charge initially at a faster rate than ones composed of Delrin, up to a similar magnitude of saturation charge density; whereas Nylon layers accumulated charge at a similar initial rate but up to a higher charge density. These data also show that freestanding layers that were polished to low R_a and R_{dq} values produced a significantly higher charge density than those grinded to high R_a and R_{dq} values using low grit grinding pads.

The methodology involved does not require the use of specialised contact materials or surface treatment in terms of TENG optimisation, beyond that of grinding and polishing, and the cleaning of samples through the use of solvents. In reinforcing the dependence of material chemical composition and surface roughness parameters on contact charging behaviour, these tests have served as a stepping stone towards fully understanding the complex role of tribology in triboelectric contacts and devices.

Acknowledgements

Special thanks to Jordan Thomas, Michael Huggan, Ryan Smith and from the Institute for Functional Surfaces technical team for crucial guidance on device construction. Paul Kilburn for the cutting, grinding and polishing of the conductive electrode samples. Rhys Moore for the additive manufacturing of the F-TENG supporting structure.

Hardy Boocock from the University of Leeds, School of Mechanical Engineering, Electronic Services for advice and guidance on construction of the electronic measurement circuit; in addition to the construction of a novel in-house feedback ammeter for initial proof-of-concept testing. Robert Guest for acquisition of the polymer samples.

Prof. Zhong Lin Wang and the staff at the Beijing Institute for Nanoenergy and Nanosystems (BINN) for providing valuable discussions and insight into the research on TENG devices.

REFERENCES

- [1] Helmholtz H. Studien über electricische Grenzschichten. *Ann Phys* 1879;243:337–82. doi:10.1002/andp.18792430702.
- [2] Harper WR. Interpretation of experiments on frictional electrification. *Nature* 1951;167:400–1. doi:10.1038/167400b0.
- [3] Wang ZL, Wang AC. On the origin of contact-electrification. *Mater Today* 2019. doi:10.1016/J.MATTOD.2019.05.016.
- [4] Fabish TJ, Duke CB. Molecular charge states and contact charge exchange in polymers. *J Appl Phys* 1977;48:4256–66. doi:10.1063/1.323412.
- [5] Matsusaka S, Maruyama H, Matsuyama T, Ghadiri M. Triboelectric charging of powders: A review. *Chem Eng Sci* 2010;65:5781–807. doi:10.1016/J.CES.2010.07.005.
- [6] Pan S, Zhang Z. Fundamental theories and basic principles of triboelectric effect: A review. *Friction* 2019;7:2–17. doi:10.1007/s40544-018-0217-7.
- [7] Harper WR. The Volta Effect as a Cause of Static Electrification. *Proc R Soc Lond A Math Phys Sci* 1951;205:83–103. doi:10.2307/98725.
- [8] Kornfeld MI. Frictional electrification. *J Phys D Appl Phys* 1976;9:1183–92. doi:10.1088/0022-3727/9/8/005.
- [9] Diaz AF, Felix-Navarro RM. A semi-quantitative tribo-electric series for polymeric materials: the influence of chemical structure and properties. *J Electrostat* 2004;62:277–90. doi:10.1016/J.ELSTAT.2004.05.005.
- [10] Zhang X-S, Han M-D, Wang R-X, Meng B, Zhu F-Y, Sun X-M, et al. High-performance triboelectric nanogenerator with enhanced energy density based on single-step fluorocarbon plasma treatment. *Nano Energy* 2014;4:123–31. doi:10.1016/J.NANOEN.2013.12.016.
- [11] Ding P, Chen J, Farooq U, Zhao P, Soin N, Yu L, et al. Realizing the potential of polyethylene oxide as new positive tribo-material: Over 40 W/m² high power flat surface triboelectric nanogenerators. *Nano Energy* 2018;46:63–72. doi:10.1016/J.NANOEN.2018.01.034.
- [12] Byun K-E, Cho Y, Seol M, Kim S, Kim S-W, Shin H-J, et al. Control of Triboelectrification by Engineering Surface Dipole and Surface Electronic State. *ACS Appl Mater Interfaces* 2016;8:18519–25. doi:10.1021/acsami.6b02802.
- [13] Pan S, Zhang Z. Triboelectric effect: A new perspective on electron transfer process. *J Appl Phys* 2017;122:144302. doi:10.1063/1.5006634.
- [14] Lee L-H. Dual mechanism for metal-polymer contact electrification. *J Electrostat* 1994;32:1–29. doi:10.1016/0304-3886(94)90026-4.
- [15] Nguyen V, Zhu R, Yang R. Environmental effects on nanogenerators. *Nano Energy* 2015;14:49–61. doi:10.1016/J.NANOEN.2014.11.049.
- [16] Nguyen V, Yang R. Effect of humidity and pressure on the triboelectric nanogenerator. *Nano Energy* 2013;2:604–8. doi:10.1016/J.NANOEN.2013.07.012.
- [17] Greason WD. Generalized model of electrostatic discharge (ESD) for bodies in approach: Analyses of multiple discharges and speed of approach. *J Electrostat* 2002;54:23–37.

- doi:10.1016/S0304-3886(01)00147-4.
- [18] von Pidoll U. An overview of standards concerning unwanted electrostatic discharges. *J Electrostat* 2009;67:445–52. doi:10.1016/j.elstat.2009.01.011.
- [19] Kiss I, Szedenik N, Berta I. Electrostatic hazard and protection: Expert system for fuel delivery modules. *J Electrostat* 2005;63:495–9. doi:10.1016/j.elstat.2005.03.008.
- [20] Yadav R, Tirumali M, Wang X, Naebe M, Kandasubramanian B. Polymer composite for antistatic application in aerospace. *Def Technol* 2020;16:107–18. doi:10.1016/j.dt.2019.04.008.
- [21] Chen J, Wang ZL. Reviving Vibration Energy Harvesting and Self-Powered Sensing by a Triboelectric Nanogenerator. *Joule* 2017;1:480–521. doi:10.1016/j.joule.2017.09.004.
- [22] Paradiso JA, Starner T. Energy Scavenging for Mobile and Wireless Electronics. *IEEE Pervasive Comput* 2005;4:18–27. doi:10.1109/MPRV.2005.9.
- [23] Fan F-R, Tian Z-Q, Lin Wang Z. Flexible triboelectric generator. *Nano Energy* 2012;1:328–34. doi:10.1016/J.NANOEN.2012.01.004.
- [24] Caillon JC. A possible unification of Newton's and Coulomb's forces. *Phys Lett Sect A Gen At Solid State Phys* 2018;382:3307–12. doi:10.1016/j.physleta.2018.09.005.
- [25] Yazdani H, Saturnino GB, Thielscher A, Knudsen K. Fast evaluation of the Biot-Savart integral using FFT for electrical conductivity imaging. *J Comput Phys* 2020;411:109408. doi:10.1016/j.jcp.2020.109408.
- [26] Yang B, Tao X, Peng Z. Upper limits for output performance of contact-mode triboelectric nanogenerator systems. *Nano Energy* 2019;57:66–73. doi:10.1016/J.NANOEN.2018.12.013.
- [27] Niu S. Theoretical systems of triboelectric nanogenerators. *Nano Energy* 2015;14:161–92. doi:10.1016/J.NANOEN.2014.11.034.
- [28] Dong Y, Mallineni SSK, Maleski K, Behlow H, Mochalin VN, Rao AM, et al. Metallic MXenes: A new family of materials for flexible triboelectric nanogenerators. *Nano Energy* 2018;44:103–10. doi:10.1016/J.NANOEN.2017.11.044.
- [29] Niu S, Liu Y, Chen X, Wang S, Zhou YS, Lin L, et al. Theory of freestanding triboelectric-layer-based nanogenerators. *Nano Energy* 2015;12. doi:10.1016/j.nanoen.2015.01.013.
- [30] Wu C, Wang AC, Ding W, Guo H, Wang ZL. Triboelectric Nanogenerator: A Foundation of the Energy for the New Era. *Adv Energy Mater* 2019;9:1802906. doi:10.1002/aenm.201802906.
- [31] Vasandani P, Mao Z-H, Jia W, Sun M. Relationship between triboelectric charge and contact force for two triboelectric layers. *J Electrostat* 2017;90:147–52. doi:10.1016/J.ELSTAT.2017.11.001.
- [32] Shao J, Jiang T, Tang W, Xu L, Kim TW, Wu C, et al. Studying about applied force and the output performance of sliding-mode triboelectric nanogenerators. *Nano Energy* 2018;48:292–300. doi:10.1016/J.NANOEN.2018.03.067.
- [33] Briscoe BJ, Sinha SK. Wear of polymers. *Proc Inst Mech Eng Part J J Eng Tribol* 2002;216:401–13. doi:10.1243/135065002762355325.
- [34] Haidar DR, Ye J, Moore AC, Burris DL. Assessing quantitative metrics of transfer film quality as indicators of polymer wear performance. *Wear* 2017;380–381:78–85. doi:10.1016/j.wear.2017.03.012.
- [35] Burris DL, Boesl B, Bourne GR, Sawyer WG. Polymeric nanocomposites for tribological applications. *Macromol Mater Eng* 2007;292:387–402. doi:10.1002/mame.200600416.
- [36] Melitz W, Shen J, Kummel AC, Lee S. Kelvin probe force microscopy and its application. *Surf Sci Rep* 2011;66:1–27. doi:10.1016/J.SURFREP.2010.10.001.
- [37] Zhai C, Chou X, He J, Song L, Zhang Z, Wen T, et al. An electrostatic discharge based needle-to-needle booster for dramatic performance enhancement of triboelectric nanogenerators. *Appl Energy* 2018;231:1346–53. doi:10.1016/j.apenergy.2018.09.120.
- [38] Avlonitis M, Kalaitzidou K. Estimating the real contact area between sliding surfaces by means of a modified OFC model. *Arch Civ Mech Eng* 2015;15:355–60. doi:10.1016/j.acme.2014.10.003.
- [39] Sedlaček M, Podgornik B, Vižintin J. Correlation between standard roughness parameters skewness and kurtosis and tribological behaviour of contact surfaces. *Tribol. Int.*, vol. 48, Elsevier; 2012, p. 102–12. doi:10.1016/j.triboint.2011.11.008.
- [40] Abdelbary A. *Wear of Polymers and Composites*. Woddhead publishing; 2015. doi:10.1016/C2014-0-03367-9.

Appendix A. Sample Topography Maps

A.1. Conductive Electrodes

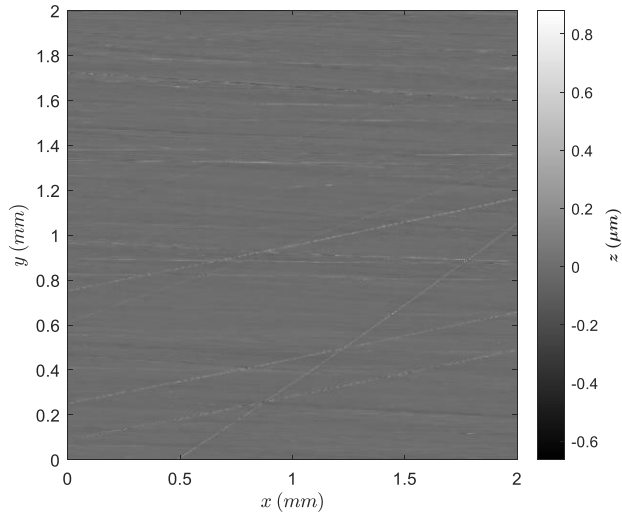


Fig. A.1. 1 – Sample topography of the Aluminium F-TENG electrode surfaces across a 2 mm by 2 mm area using a Bruker NPFLEX white light interferometer.

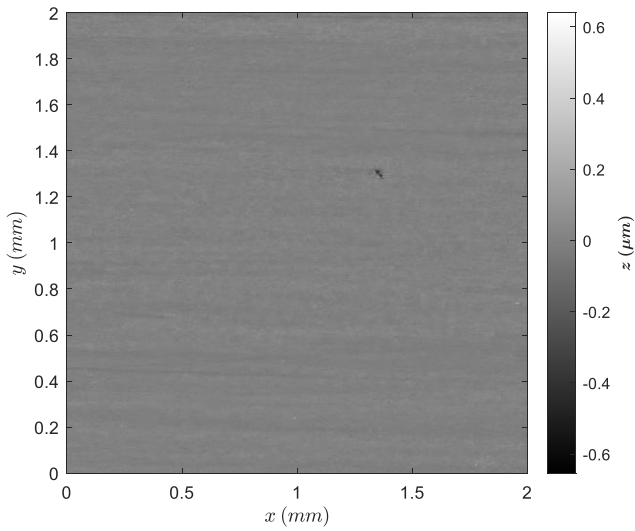


Fig. A.1. 2 – Sample topography of the Aluminium F-TENG electrode surfaces across a 2 mm by 2 mm area using a Bruker NPFLEX white light interferometer.

A.2. Triboelectric Polymers

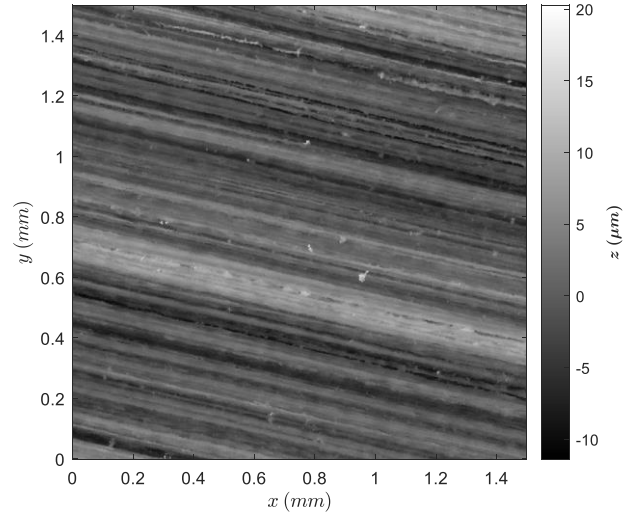


Fig. A.2. 1 – Sample topography of the Nylon F-TENG sample surfaces across a 1.5 mm by 1.5 mm area using a Bruker NPFLEX white light interferometer after being subjected to a grinding process using 120 grit SiC pads.

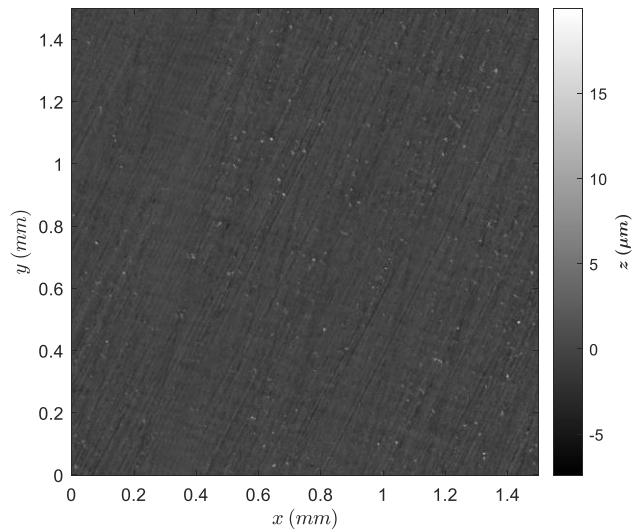


Fig. A.2. 2 – Sample topography of the Nylon F-TENG sample surfaces across a 1.5 mm by 1.5 mm area using a Bruker NPFLEX white light interferometer after being subjected to a grinding process using 600 grit SiC pads.

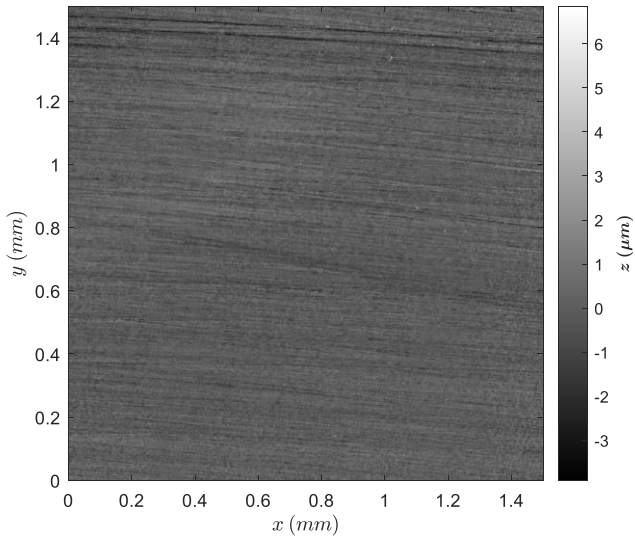


Fig. A.2. 3 – Sample topography of the Nylon F-TENG sample surfaces across a 1.5 mm by 1.5 mm area using a Bruker NPFLEX white light interferometer after being subjected to a grinding process using 800 grit SiC pads.

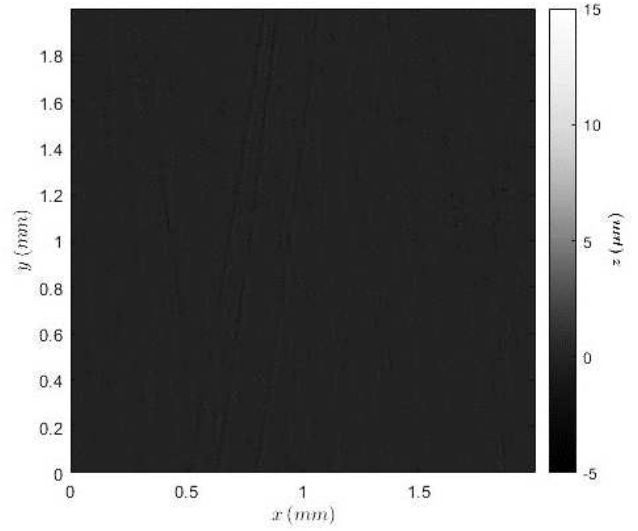


Fig. A.2. 5 – Sample topography of the Nylon F-TENG sample surfaces across a 2 mm by 2 mm area using a Bruker NPFLEX white light interferometer after being subjected to a grinding process using 1200 grit SiC pads and then polished using a diamond suspension.

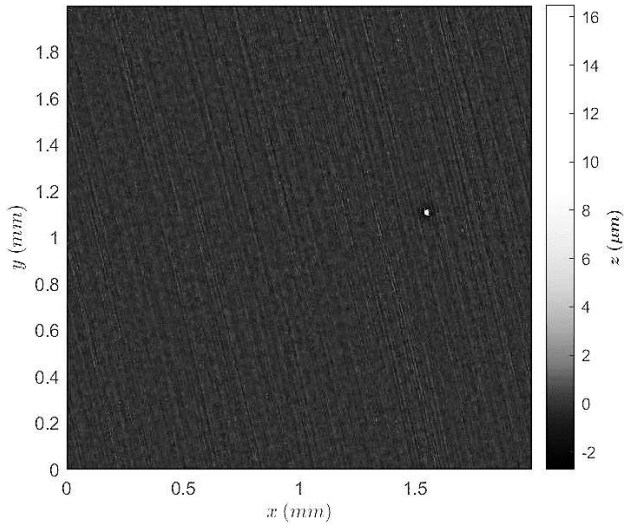


Fig. A.2. 4 – Sample topography of the Nylon F-TENG sample surfaces across a 2 mm by 2 mm area using a Bruker NPFLEX white light interferometer after being subjected to a grinding process using 1200 grit SiC pads.

Appendix B. Sample Gradient Maps

B.1. Conductive Electrodes

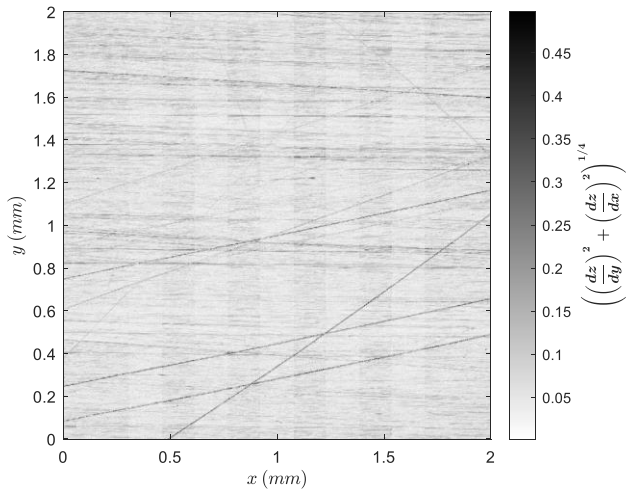


Fig. B.1. 1 – Square-root colour-scaled gradient map of the Aluminium F-TENG electrode surfaces across a 2 mm by 2 mm area using a Bruker NPFLEX white light interferometer.

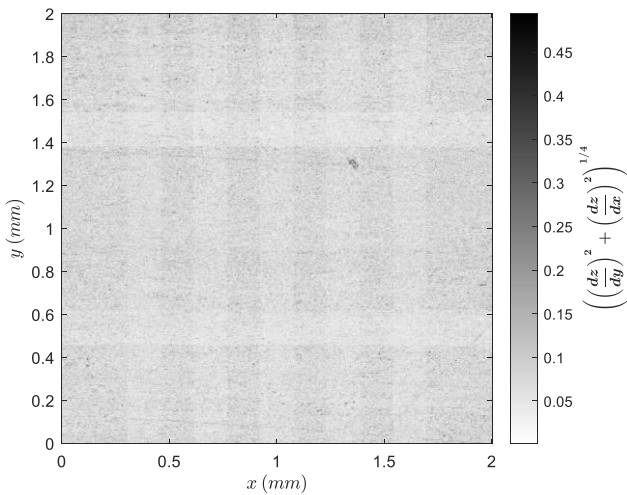


Fig. B.1. 2 – Square-root colour-scaled gradient map of the Aluminium F-TENG electrode surfaces across a 2 mm by 2 mm area using a Bruker NPFLEX white light interferometer.

B.2. Triboelectric Polymers

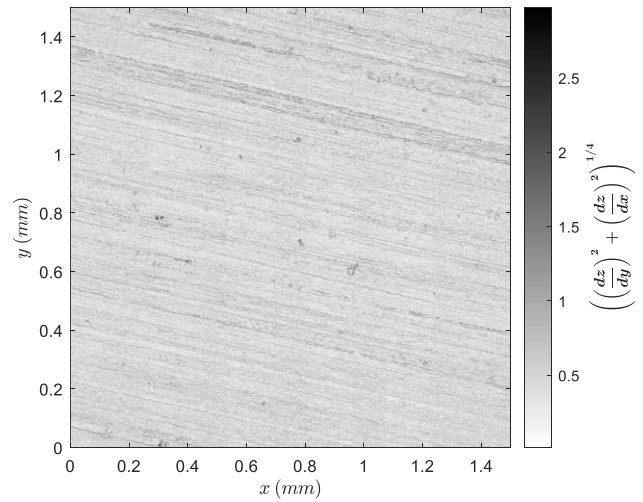


Fig. B.2. 1 – Square-root colour-scaled gradient map of the Nylon FTENG sample surfaces across a 1.5mm by 1.5mm area using a Bruker NPFLEX white light interferometer after being subjected to a grinding process using 120 grit SiC pads.

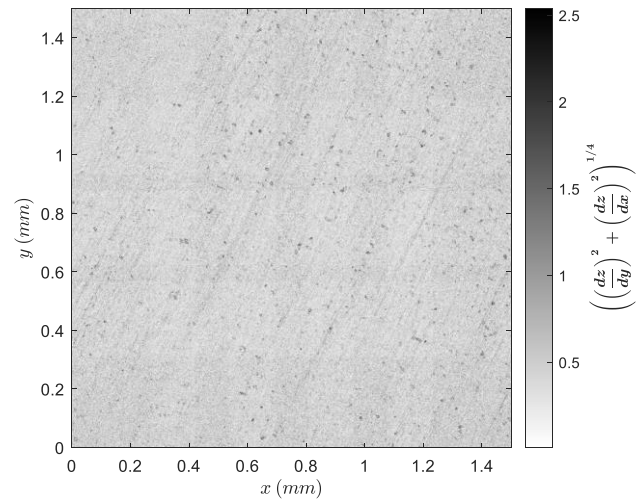


Fig. B.2. 2 – Square-root colour-scaled gradient map of the Nylon F-TENG sample surfaces across a 2mm by 2mm area using a Bruker NPFLEX white light interferometer after being subjected to a grinding process using 600 grit SiC pads.

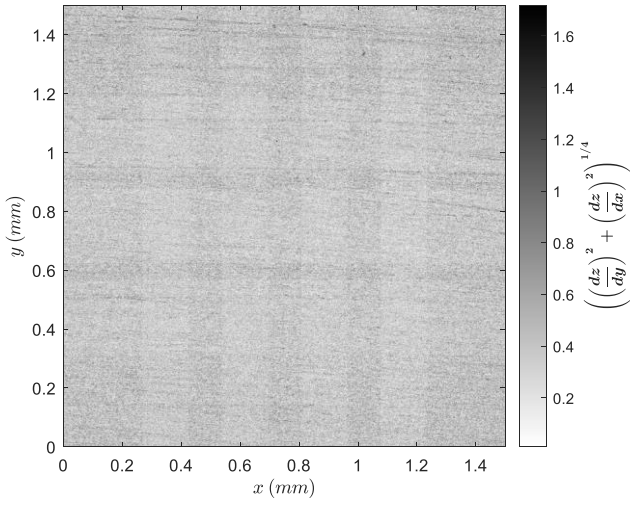


Fig. B.2. 3 – Square-root colour-scaled gradient map of the Nylon F-TENG sample surfaces across a 1.5mm by 1.5mm area using a Bruker NPFLEX white light interferometer after being subjected to a grinding process using 800 grit SiC pads.

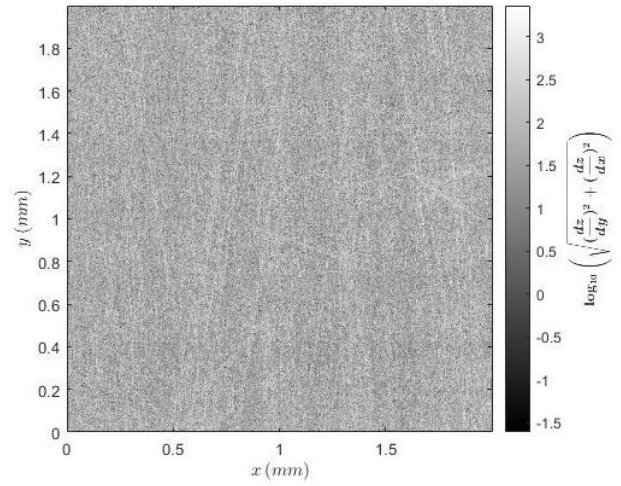


Fig. B.2. 5 – Logarithmically colour-scaled gradient map of the Nylon F-TENG sample surfaces across a 2mm by 2mm area using a Bruker NPFLEX white light interferometer after being subjected to a grinding process using 1200 grit SiC pads.

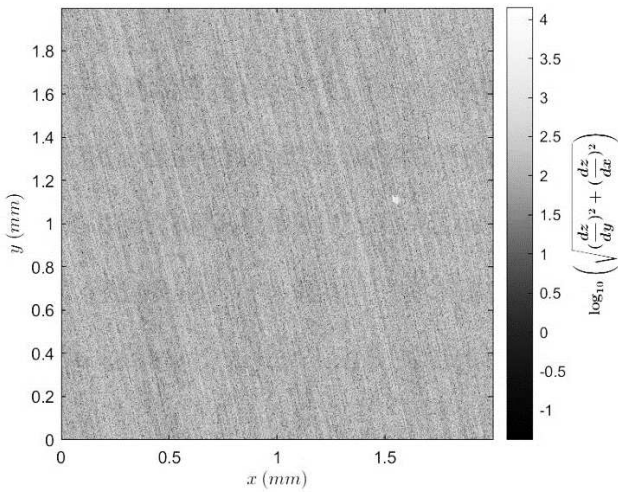


Fig. B.2. 4 – Logarithmically colour-scaled gradient map of the Nylon F-TENG sample surfaces across a 2mm by 2mm area using a Bruker NPFLEX white light interferometer after being subjected to a grinding process using 1200 grit SiC pads.